Title: Beyond land surface temperature: identifying areas of daytime thermal discomfort in cities by combining remote sensing and field measurements.

Authors: Julie C. Fahy[a,b], Christoph Bachofen[c,d], Reto Camponovo[e], Peter Gallinelli[e], Martin A. Schlaepfer[a]

[a] Institute for Environmental Sciences, University of Geneva, Geneva, Switzerland

[b] Ecology and Aquatic Systems Engineering group, HEPIA, University of Applied Sciences and Arts Western Switzerland, Lullier, Switzerland

[c] Plant Ecology Research Laboratory PERL, School of Architecture, Civil and Environmental Engineering, EPFL, Lausanne, Switzerland

[d] Functional Plant Ecology, Community Ecology Unit, Swiss Federal Institute for Forest, Snow and Landscape WSL, Lausanne, Switzerland

[e] Environment, Climate, Energy and Architecture Laboratory, HEPIA, University of Applied Sciences and Arts Western Switzerland, Geneva, Switzerland

Corresponding author: Martin A. Schlaepfer (martin.schlaepfer@unige.ch)

Highlights:

- We measured thermal discomfort of pedestrians using a portable weather station

- Model outputs produce reliable fine-grained maps of daytime thermal discomfort

- LCZ and solar energy explain most of the variability in thermal discomfort

- Land surface temperature is an unreliable proxy for thermal discomfort.

Satellite images of land surface temperatures (LST) are commonly used to identify areas within cities most prone to diurnal thermal discomfort, but they may not reflect the experiences of pedestrians. Here, we developed predictive statistical models for Physiological Equivalent Temperature (PET), an indicator of thermal discomfort, with easily accessible spatial predictors. For this, we measured PET (n = 4472) along eight transects (range: 700-5000 meters) using a multi-sensor instrument in the urban fabric of Geneva, Switzerland during periods of summer heat. We parametrised generalised additive models (GAM) and linear mixed models (LMM) with six commonly available predictor variables [*solar energy, Local Climate Zone (LCZ), albedo, LST, Normalized Difference Moisture Index (NDMI)* and *canopy cover*]. We found that LST, alone, explained < 2% of observed variation in PET, whereas the GAM with all the 6 predictor variables had $R^2 = 0.43$. LCZ and solar energy explained most of the variability of PET across the city. PET values were lower in the densely built city centre than in the peri-urban environment. LST is poorly correlated with air temperature and PET in urban settings, and thus should not be used alone to predict outdoor thermal discomfort.

Keywords: Generalised additive model; Landsat; Sentinel-2; Land surface temperature; NDVI; Thermal comfort; Urban heat island; Physiological Equivalent Temperature

1. Introduction

The air temperature in urban ecosystems is several degrees Celsius higher than in the non-urban environment (Urban Heat Island, UHI)(Oke, 1982; Oke et al., 2017). The higher air temperatures are caused by large energy outputs from combustion engines and energy-storing building materials that capture and subsequently release heat and trapped radiation (Stewart & Oke, 2012). Global warming, combined with increased densification of urban centres, will likely exacerbate the magnitude of the UHI in the future (Kundu & Pandey, 2020). This is expected to have occasional positive effects such as reduced heating needs and lower cold-related mortality in winters, but also negative effects such as increased energy demand for cooling and thermal discomfort during summer heatwaves (Huang et al., 2023; Iungman et al., 2023).

The consequences of thermal discomfort during periods of prolonged heat can range from a mild nuisance to death, depending on the severity of the phenomenon and the susceptibility of the individual (Armstrong et al., 2019; Ragettli et al., 2017). For instance, the extreme 2003 heatwave led to an increase of 141% mortality in Paris, whereas smaller towns in France had a 40% excess mortality (Dousset et al., 2011). A demographic shift towards elderly age-classes in numerous cities of industrialised countries (Anderson & Hussey, 2000) is expected to make the urban population generally more vulnerable to thermal discomfort. Consequently, mitigation of thermal discomfort has become a major public health issue (Armstrong et al., 2019; Ragettli et al., 2017).

Thermal discomfort includes the perceived physiological and psychological stress caused by heat. Several indices have been developed to calculate thermal discomfort, such as the Universal Thermal Climate Index (UTCI Bröde et al., 2012; Fiala et al., 2012) and the Physiological Equivalent Temperature (PET Höppe, 1999). The theoretical framework of

thermal discomfort indices differ slightly, but both rely on similar environmental factors (ambient air temperature, wind speed, solar radiance, and relative humidity) and are strongly correlated with one another (Blazejczyk et al., 2012; Fang et al., 2019; Lai et al., 2020; Zare et al., 2018). Thermal discomfort indices are, in theory, better suited for predicting the sub-lethal undesirable effects of heat than air temperature alone (Lai et al., 2020; Zhang et al., 2014) but see (Armstrong et al., 2019) regarding the specific case of predicting heat-related mortality].

Cities are spatially heterogeneous with regard to thermal discomfort, and urban planners therefore will need to focus mitigation efforts in neighbourhoods or micro-environments that generate the greatest thermal discomfort (Makido et al., 2019). Mean air temperature and PET values can vary by >10 °C both across neighbourhoods and on smaller spatial scales (Klok et al., 2019; Liu et al., 2018). Although indoor and nocturnal thermal discomfort likely also play an important role from a public health perspective (Ormandy & Ezratty, 2016; van Hove et al., 2015), it will be useful, as a first step, to identify parts of a city that are most likely to experience extreme thermal discomfort outdoors during the day.

Several environmental factors can potentially attenuate thermal discomfort in cities. Shading of solar irradiance can result in decreases in 15-20°C PET (Gulyás et al., 2006; Klok et al., 2019) within a city depending on the extent of shading from buildings and vegetation. Other studies have suggested that air temperature or thermal discomfort are positively correlated with materials with low albedo (Santamouris, 2014), high air humidity (Shashua-Bar & Hoffman, 2000), low tree coverage (Bowler et al., 2010; Lehmann et al., 2014; Shashua-Bar & Hoffman, 2000), the aspect-ratio of buildings (the height of buildings in relation to their spacing) (Bartesaghi-Koc et al., 2019; Kakon et al., 2010), sky-view factor (He et al., 2015) and the proportion of sealed surfaces (Lehmann et al., 2014). Missing, to date, is a relatively simple, spatially explicit statistical model that integrates key predictors of thermal discomfort over an entire urban area and that can be potentially implemented by non-specialists.

Land surface temperature (LST) has been proposed a suitable urban indicator with a "direct relationship with human health and living comfort" (Chaudhuri & Kumar, 2020). LST is calculated from radiation measured by satellite, is freely available, regularly updated and presents the advantage of covering entire cities. It has therefore been frequently used as a proxy for urban air temperatures and thermal discomfort (Chaudhuri & Kumar, 2020; Deilami et al., 2018; Tomlinson et al., 2011; Venter et al., 2020; Weng et al., 2004). For instance, among the 75 studies on UHI reviewed by Deilami et al. (2018), 44% used satellite-derived LST alone to characterise the UHI effect. LST has also been used to measure the putative effects of different types of vegetation on air temperature (Schwaab et al., 2020) and along with surface albedo and imperviousness or urban density as a proxy for thermal comfort (Chrysoulakis et al., 2014). A theoretical limitation is that LST only accounts for surface radiation (Voogt & Oke, 2003). While radiation can increase air temperatures above the surface, this effect quickly decreases within a few centimetres above the surface, so that temperatures measured at human height are significantly lower than near-surface measurements (May & Oliphant, 2023). In addition, a low spatial resolution of 100 m (downscaled to 30 m with Landsat 8) implies that measurements may be influenced by adjacent rooftops, solar panels, or canopy tops, which could result in an overestimation of the temperature experienced by pedestrians at street level (Kamath et al., 2023; Parlow et al., 2014).

To refine thermal climate predictions within urban settings the Local Climate Zones (LCZ) framework was developed (Stewart & Oke, 2012). LCZ categories include 10 different *built types* that capture variation in density, height, and spacing of buildings. These categories can be further sub-divided into seven *land-cover types* that vary in extent and height of vegetation, extent of impervious surfaces and presence of water (e.g., Oke et al., 2017). Although several studies have reported significant differences in mean air temperature between LCZ categories (Alexander & Mills, 2014; Aminipouri et al., 2019; Geletič et al., 2018; Liu et al., 2018; Stewart

et al., 2014) the ranking of LCZ categories by mean temperature have been inconsistent. LCZ categories are quantified at the scale of city blocks, and as such, indirectly capture the effects of vegetation, impervious surfaces, etc. at a larger scale (e.g., the cumulative cooling effects that arise from high tree density in each neighbourhood).

Here, we question whether LST and LCZ estimates, alone, are sufficient to predict PET within an urbanised setting, and assess the extent to which available remote sensing information [albedo, Normalized Difference Moisture Index (NDMI), Normalized Difference Vegetation Index (NDVI), canopy cover, surface imperviousness, and solar energy] can improve such PET predictions. To test this, we developed spatially explicit regression models of thermal discomfort by leveraging detailed, publicly available geospatial information for the city of Geneva (Switzerland) and fine-scale field measurements of climate variables necessary to calculate PET. The goal was therefore to generate a spatially explicit representation of PET that will indicate which parts of the city are typically the most likely to generate situations of thermal discomfort.

2. Methods

2.1 Study area

The study area focuses on the urban component of Geneva, Switzerland (46º 12' N, 6º 09' E). The climate in Geneva is a temperate oceanic climate (Köppen classification: Cfb) with cool winters and warm summers (mean annual temperature: 11.0 ºC, mean annual precipitation 946 mm, years 1991–2020, Cointrin weather station, www.meteosuisse.admin.ch). The city is located where the Rhone River exits Lake Geneva and is surrounded by low mountain ranges to the north, west and south. The city centre is characterised by the old town, with narrow

shaded cobbled streets, and by a peri-urban ring composed of more recent neighbourhoods with residential and business buildings, small parks and a limited number of large open areas.

2.2 Field and remote sensing data

2.2.1 Field assessments of thermal discomfort

We calculated the thermal discomfort based on fine-scale measurements of air temperature (T_{air}), relative air humidity (RH), surface temperature (T_{surf}), solar energy (Gh) and windspeed (WS) that were collected with a portable climate station, the microclimate-meter (Table S1, Figure 1). Details regarding sensors are found in the Supplementary Materials and Gallinelli et al (2017). Sensor measurements took place each second (i.e., roughly once per meter at a walking pace) to provide a detailed spatial representation of area on the scale of the street to the neighbourhood. Measurements were collected along eight transects across the city of Geneva during hot summer days in 2018 and 2019, between midday and 5 pm (Figure 1,

Table *1*) and lasted roughly 1-1.5h each. Some transects were spatially similar but walked on different days to capture within-site variability.

Figure 1: A. Portable climate station; B. Study area, with the location of transects (black lines), LCZ categories (described in Table 3) and the position of Geneva (arrow pointing to red dot) and Switzerland (black outline) within Europe (inset).

As an index for thermal discomfort, we selected the Physiological Equivalent Temperature (PET), which has been used in a variety of situations and regions (Potchter et al., 2018; Walther & Goestchel, 2018) and shows good correspondence between simulations and ground truthing (Coccolo et al., 2016). The PET index was calculated based on Höppe (Höppe, 1999; Sadeghipour Roudsari, 2024) for an average middle-aged (40 yrs, 1m80) man walking along the street in summer clothes.

Table 1: Transect characteristics.

Transect	Date	Start time	End time	Length (m)	Min PET (°C)	Max PET (°C)
Acacias-Aire	13.06.19	13:10	14:15	5849	23.2	35.9
Bastions	26.07.18	16:44	17:18	1916	29	48.6
EV-Cologny	13.06.19	11:26	12:30	5760	16.5	33.3
Fontaines	27.07.18	14:16	15:17	10347	23.8	41.8
Parcs	26.07.18	14:30	15:13	2581	25.9	40.8
Plainpalais	26.07.18	16:45	17:18	2164	28.7	47.2
StJean	19.07.18	14:42	16:38	4746	24.8	42.8
StJean	20.07.18	13:10	14:25	4400	25.1	40.9
Vernets	27.07.18	14:08	14:54	4650	23.0	43.4
Vernets	08.08.18	13:31	14:36	4119	25.8	43.0

2.2.3 Remote sensing data

As spatial predictors of PET we selected eight remote sensing variables that (i) had supporting evidence of a functional link with thermal discomfort and ii) covered the entire urban area of the centre of Geneva (Table 2, and see maps of each indicator Figure S1). Details on data acquisition and methodological choices for each geospatial layer is provided in the Supplementary Materials (Notes S1). Local climate zones (LCZ) were generated for the entire canton of Geneva following Stewart and Oke (2012). 18 LCZ types were initially identified in

the study area. Following Liu et al. (2018), some LCZ categories were merged based on their similar phenotypes or shared thermal properties to limit the number of categories (

Table *3*). The variable *Solar Energy* is the output of an independent 3D model that captures in the influence of topography, slope, standing vegetation and buildings. Thus, it captures the key role of shading (Supplementary Materials, Note S1).

Explanatory variables were prepared in ArcGIS Pro (Version 2.5.1) to be combined into a table with an output resolution of 10 m to be later used for the prediction of PET over the entire study area. Values from all raster data were extracted onto points forming a 10*10m grid. For each raster, the value of the unique cell in which the grid point was located was attributed to that point. All variables were linearly interpolated to downscale to a 10 m resolution. Evapotranspiration (from MODIS) was not integrated because it was considered unreliable in urban environments.

Table 2: Source and spatial resolution of all nine explanatory variables initially considered for PET.

Variable	Source	Unit [range]	Spatial resolution (m)
Albedo	Estimation with Sentinel-2	unitless [0, 1]	20
Mean summer LST	Estimation with data from Landsat 8	°C [20, 44]	30 (resampled from 100 m)
Normalized Difference Moisture Index (NDMI)	Estimation with data from Sentinel-2	Unitless [-1, 1]	20

Normalized Difference Vegetation Index (NDVI)	Estimation with data from Sentinel-2	Unitless [-1, 1]	20
Percentage of canopy cover per 100 m^2	Local canopy model obtained from LiDAR	% [0-100]	10
Percentage of impervious surfaces per 100 m^2	Public GIS repository (https://ge.ch/sitg/)	% [0-100]	10
Solar energy (sum of irradiance in July)	Public GIS repository (https://ge.ch/sitg/)	kWh m^{-2} [0, 188]	0.5
Local Climate Zones (LCZ)	Manually designated using the typology by Stewart and Oke (2012)	Categorical (n = 9)	0.02 - 67 ha

Table 3: LCZ Number, LCZ types defined in Steward and Oke (2012), and the corresponding surface area in the study perimeter, Geneva Switzerland.

Number	LCZ type	Descriptor	Sum of surfaces (ha; % total)
1	A+G	Dense trees and Water	141 (7.59)
2	B+BC+BD	Scattered trees; Scattered trees, bush and shrub; Scattered trees and low plants	72 (3.90)
3	D+C	Low plants; Shrub and scrub	8 (0.42)
4	9	Sparsely built	186 (10.01)
5	6+8D	Open low-rise; Large low-rise and low plants	126 (6.78)

6	5+2A+ 2B	Open mid-rise; Compact mid-rise and dense trees; Compact mid-rise and scattered trees	786 (42.29)
7	4	Open high-rise	6 (0.30)
8	1+2	Compact high-rise; Compact mid-rise	363 (19.50)
9	8+E	Large low-rise; Bare rock or paved	171 (9.21)

2.3 PET predictions using regression models

To predict PET across the urban component of Geneva, we parametrised Generalised Additive Models (GAMs) and Linear Mixed Models (LMMs) of measured PET with the remote sensing data using R functions *gam* and *lmer*, respectively (R core team, 2023). GAMs allow for non-linear relationships between predictor variables and the measured PET. To limit overfitting, we restricted the degrees of freedom for the regression spline to k = 4. Linear mixed models (LMMs) may explain less of the observed variation if relationships are non-linear, but they present the advantage that parameters can be provided for predictive equations. For both GAM and LMM we used the same predictors and model structure, except for *Albedo*, which was log-transformed for the LMM to reduce the heteroscedasticity. LCZ categories were treated as non-ordered factors. The variables *Transect* and *Date* were used as random effects to account for differences in meteorological conditions. Moreover, we examined if the addition of tensor splines that account for spatial autocorrelation between measurements improved the prediction. The R function *yhat* was used for variance partitioning of predictor variables (Ray-Mukherjee et al., 2014).

As the highest resolution of remote sensing data was 10 m (Table 2), we averaged the measured PET to the same spatial resolution. This resulted in 4472 observations of PET across all

transects. We used a random sample of 80% of the measured PET for parametrising the regression models, and the remaining 20% for validation.

Four *a priori* models were compared: a full model composed of all the significant predictor variables after model selection ("Selected" model); a reduced model composed solely of predictor variables that are generally readily available via remote sensing ("Easy-access" model); a model with only LCZ as predictor variable ("LCZ") and a model with only LST as predictor variable ("LST"). We performed model selection of the "Selected model" based on the AIC using the *step* function. The four models were compared with the goodness of fit of the 20% of validation data. As Goodness-of-Fit indicators, we used the percentage of bias between measured and predicted PET, the nash-sutcliffe efficiency (NS efficiency) and the root mean squared error (RMSE). The NS efficiency ranges from $-\infty$ to 1, with 1 being a perfect fit of predicted and measured PET, 0 indicating that the simulated data are as accurate as the mean of the measured data, and values below 0 indicating that the predicted data are less accurate than the mean of the measured data. The spatial prediction from each model was visually assessed for plausibility considering the authors' personal knowledge of the city's microclimate.

3. Results

Thermal discomfort (PET) variation across the city

Across all transects, PET ranged from 16.5–48.6 ºC and varied by 12.7–20.4 °C within transects (

Table *1*), indicating high variance of thermal discomfort within the urban centre of Geneva on any given day. Within transects, PET measurements were highly correlated with air temperature measurements (mean across transects and dates: ρ = 0.43) but only weakly correlated with LST (ρ = 0.06, Fig. S2).

GAM and LMM performance

The *NDVI* and the proportion of *Impervious Surfaces* did not significantly contribute to explaining the variability of PET during model selection and were therefore removed from the GAM and LMM. *NDVI* was highly correlated with *NDMI* (ρ = 0.51; Fig. S3), which explained a higher fraction of the variability and was therefore selected for the model. As a result, the "Selected" model included six predictor variables and the "Easy access" model four predictor variables (Table 4).

The Selected model (R^2 = 0.42) and Easy-access model (R^2 = 0.41) performed almost equally well in capturing the variation of PET measured along the transects. The spatial representation of predicted PET values across the city are nearly identical (Table S2). Validation with the 20 % of remaining PET measurements showed that the Selected model was able to predict PET relatively well (NS-efficiency of 36%), had an extremely low bias (1%), and it had the lowest RMSE of all models (Table 4). The Goodness-of-Fit is slightly lower in the Easy-access model, with a slightly lower NS-efficiency (33%) and a slightly higher RMSE (3.65). By contrast, the models with only LST and only LCZ perform relatively poorly (Table 4). Most of the variation was contained in the random effect for these last two models.

Table 4: Summary of Goodness-of-Fit for General Additive Models (GAMs) to predict Physiological Equivalent Temperature (PET).

Model Name	Variables	Goodness-of-Fit			
		R^2	RMSE	Percent Bias	NS efficiency
Selected GAM	Fixed effects: *Albedo, Canopy Cover*, *Solar Energy*, *LST*, *NDMI*, *LCZ* Random effects: *Date, Transect*	42.8 %	3.57	0.01	0.36
Easy access GAM	Fixed effects: *Albedo, LST*, *NDMI*, *LCZ* Random effects: *Date, Transect*	41 %	3.65	0.01	0.33
LCZ GAM	Fixed effect: *LCZ* Random effects: *Date, Transect*	34.7 %	3.78	0.01	0.28
LST GAM	Fixed effect: LST Random effects: *Date, Transect*	30.5 %	3.77	0.01	0.28
Selected LMM	Fixed effects: *Albedo, Canopy Cover*, *Solar Energy*, *LST*, *NDMI*, *LCZ* Random effects: *Date, Transect*	fixed effects: 11.1 % random effects: 48.0 %	3.61	0.01	0.34
Easy access LMM	Fixed effects: *Albedo, LST*, *NDMI*, *LCZ* Random effects: *Date, Transect*	fixed effects: 9.3 % random effects: 47.1 %	3.66	0.01	0.33
LCZ LMM	Fixed effect: *LCZ* Random effects: *Date, Transect*	fixed effects: 5.4 %	3.78	0.01	0.28

LST LMM	Fixed effect: LST	random effects: 45.9 %			
		fixed effects: < 1 %	3.77	0.01	0.28
	Random effects: *Date, Transect*	random effects: 41.9 %			

Variance partitioning of the Selected GAM illustrates that PET is explained primarily by LCZ and Solar Energy in July. Albedo, Canopy Cover and NDMI have a more modest explanatory power, whereas LST is marginal (Table 5).

Table 5: Variance partitioning of significant factors in Selected GAM model of PET.

Factor	Relative Importance [%]
LCZ	7.32
Solar Energy	3.58
Albedo	2.44
Canopy Cover	1.61
NDMI	1.54
LST	0.13

Model structure: random effects and tensor spline

As expected, the random effects *Date* and *Transect* explained a large proportion of the observed variability of PET in the GAM models because they capture the important temporal and spatial variations in air temperature, humidity and radiation. The tensor spline captured patterns of

spatial autocorrelation and significantly improved the model fit of both the parametrisation and validation data (R^2 values were roughly 10 % higher), but visual inspection of its graphical representation strongly suggests that the tensor spline overfit the data. Indeed, predicted values rapidly became unrealistic within the study perimeter with increased distance from sampled transects (Table S3). We therefore did not include a tensor spline in the final model comparisons.

Relationship between measured PET and model predictors

The functional response curves of individual predictor variables generally match the expected theoretical   relationship   with   PET   (
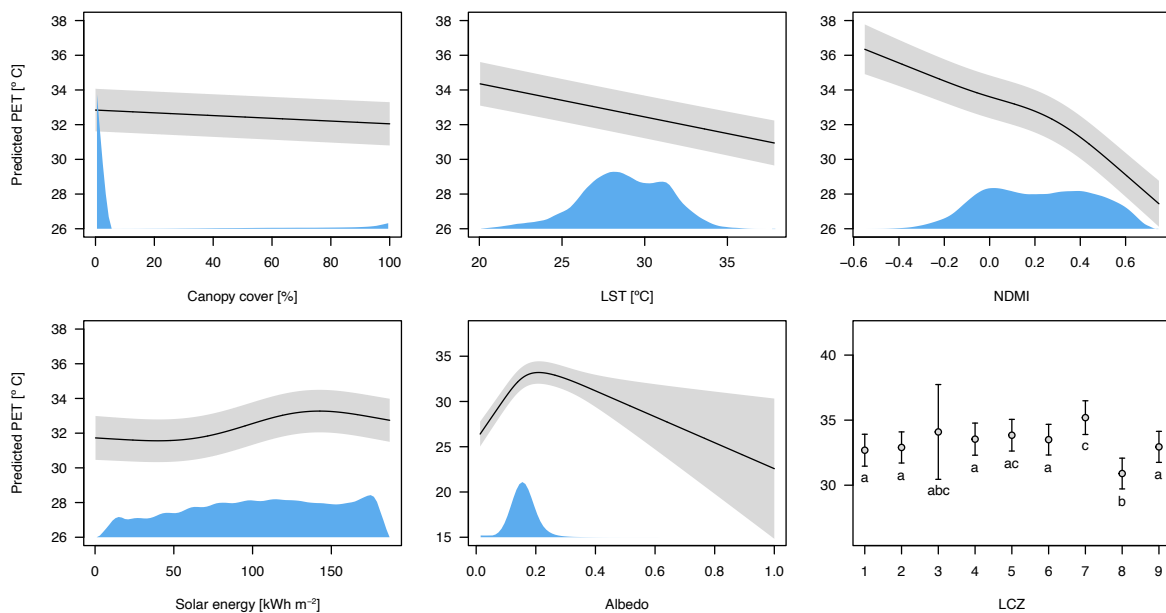
Figure *2*). PET correlates negatively with increasing *Canopy Cover* and *NDMI*, and correlates positively with *Solar Energy in July*. As expected, LCZ 7 (Open High Rise) and 5 (Open Low Rise, Large Low Rise with low plants) were associated with high PET, whereas LCZ 8 (Compact High Rise and Compact Mid Rise) was associated with low PET (Fig 4). LCZ 3 (Low Plants) had a large variation. LST correlates negatively with PET, which, at first glance, is unexpected and appears contradictory, but likely reflects that some of the highest LST values occur in the old town where the satellite measurement may capture high roof-top temperatures, whereas PET at pedestrian height within the narrow, shaded, cobble-stone roads is relatively

cool. The functional response between *Albedo* and PET is positive in the range of values where most observations occur, but then decreasing, somewhat surprisingly, with an increasing standard error (
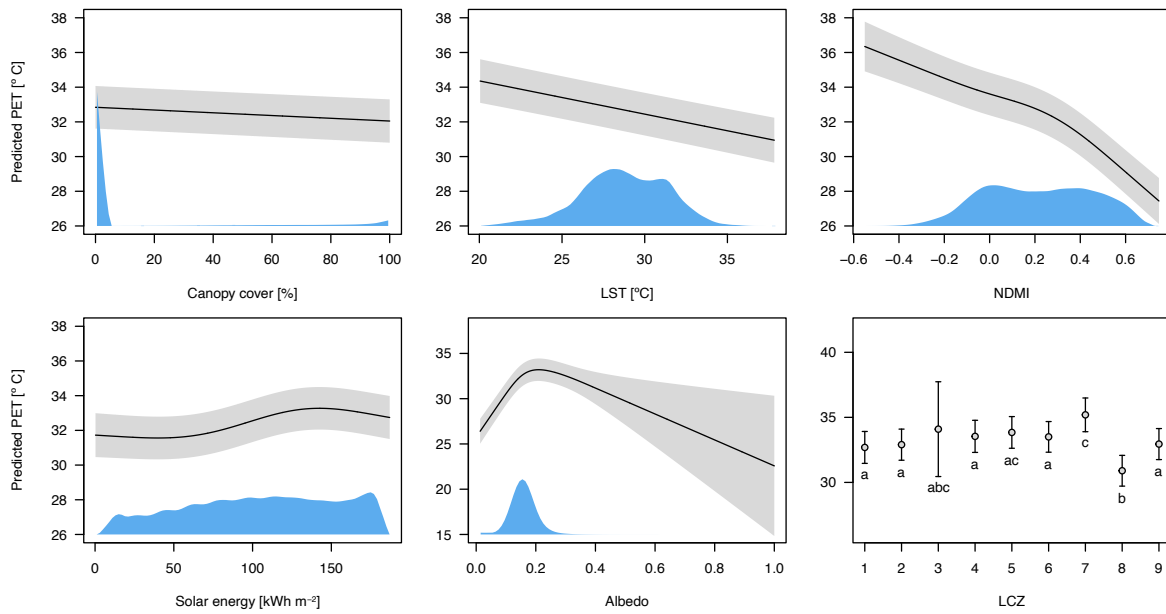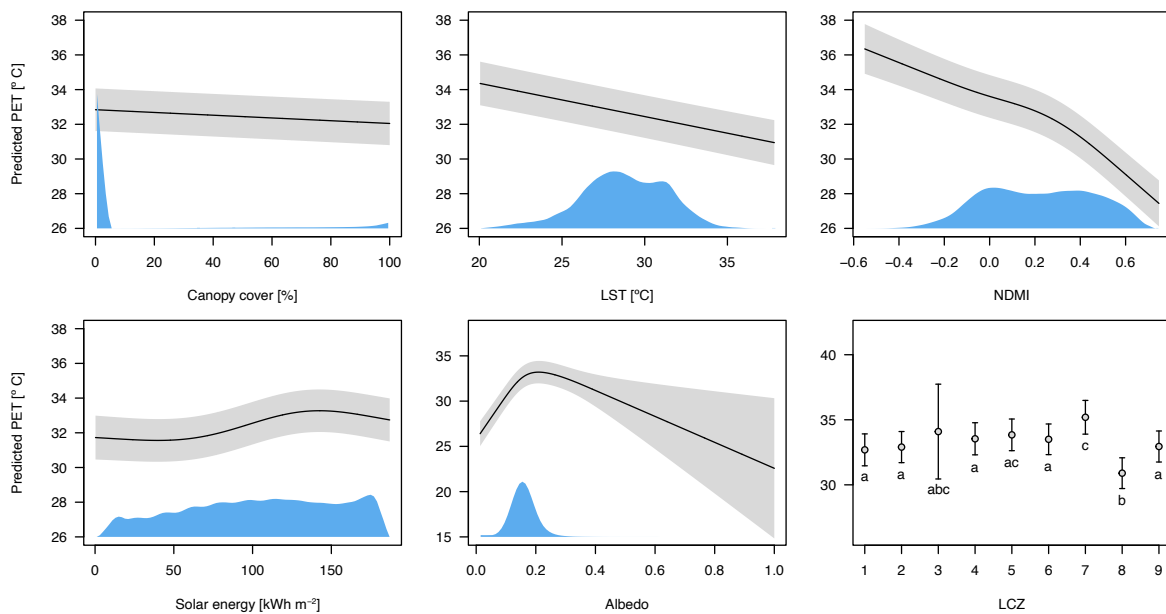
Figure *2*).

Figure 2: Predicted PET over the range of the six explanatory variables (prediction standard error in grey) for the Selected GAM. The blue areas show the density distribution of the predictors across their interval. Letters indicate pairwise comparisons of the effect of LCZ (p

< 0.05). Note that the y axis differs for albedo and LCZ, and that LCZ category numbers differ from Stewart and Oke (2012) (see Table 3).

Spatial predictions of PET in urban sections of Geneva

The PET predicted with the Selected GAM for the urban part of Geneva (
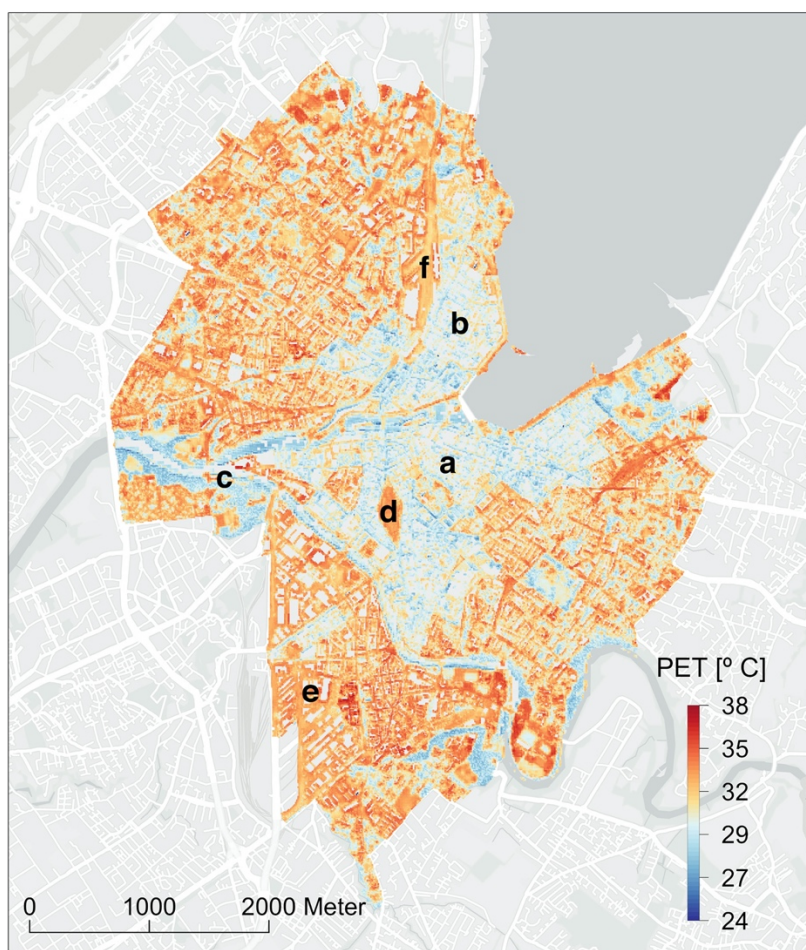
Figure *3*) not only shows a good correspondence with field measurements along transects (Table S2), but also conforms with our experience of the micro-climatic variations within the city. For example, PET is predicted to be relatively low in the narrow streets of the old town (a), the dense Pâquis neighbourhood (b), and sections along the large Rhône and Arve rivers

(c). Conversely, PET values are predicted to be relatively high in the large, unshaded, barren Plaine de Plainpalais (d), the industrial zone of La Praille (e), and along the railway tracks near the main train station (f). The model also performs well at a smaller spatial scale: within a park (Parc des Eaux-Vives, Figure 5) it captures the relatively hot clay tennis courts (where Tomas Machac famously defeated Novak Djokovic on 24 May 2024) (g), a hot adjacent street (Quai Gustave Ador; h), relatively warm open, sunny lawn areas (i), and cool areas under the large trees (j). PET within the Eaux-Vives park ranges from 27.3 to 37.3 ºC (Figure 5).
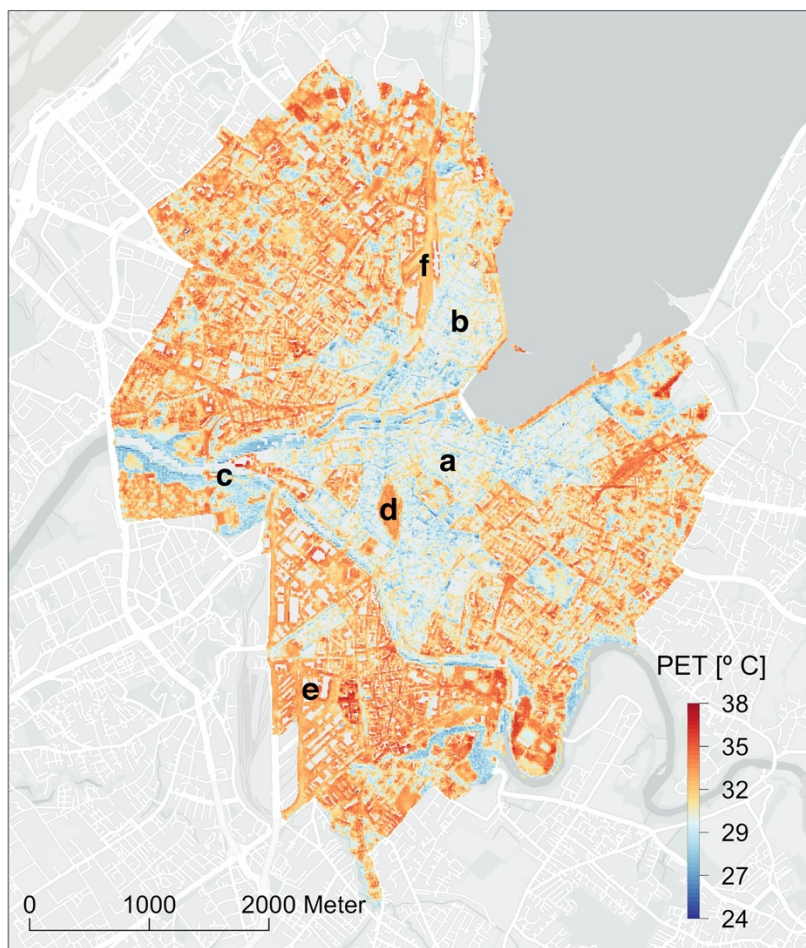
Figure 3: Predicted Physiological equivalent temperature (PET) across the urban fabric of Geneva during daytime in summer using the "Selected" GAM model. Letters refer to panels in Figure 4.
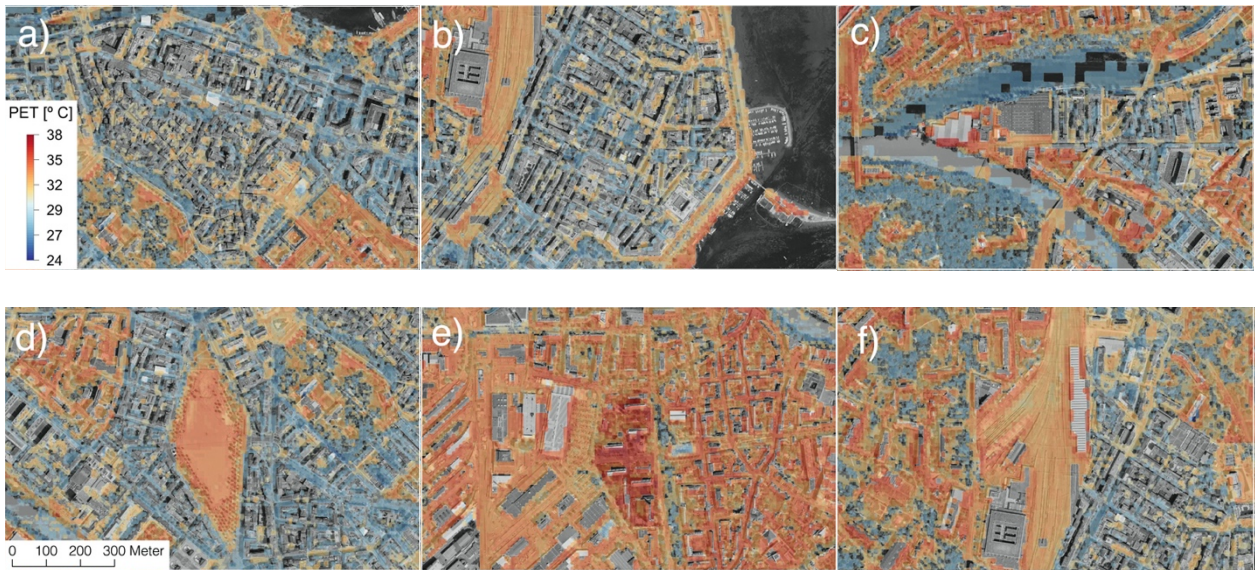
Figure 4: Predicted Physiological equivalent temperature (PET) in selected locations in the city of Geneva during daytime in summer : a) old town with narrow streets, b) the dense Pâquis neighbourhood, c) the junction of the Rhone and Arve rivers, d) the large, unshaded, Plaine de Plainpalais, e) the industrial zone of La Praille, and f) railways near the main train station.
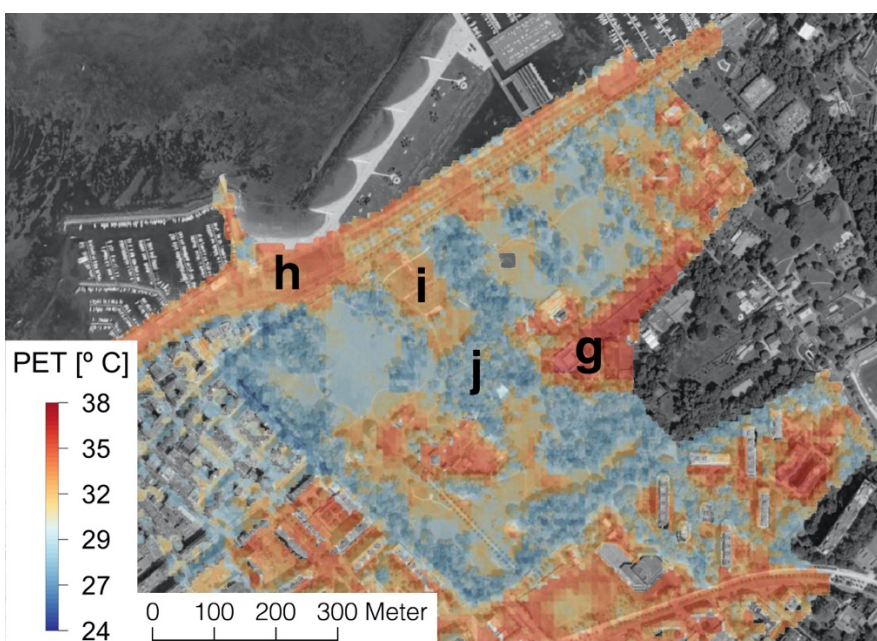
Figure 5: Predicted Physiological equivalent temperature (PET) in the Parc des Eaux-Vives in Geneva during daytime in summer, overlayed on spatial features of the park. g) relatively hot tennis courts, h) hot adjacent street, i) warm open sunny lawns, j) cool areas under large trees.

The Selected Model's spatial predictions yielded superior results to other simpler models (Figure 6). The LCZ model is spatially coarse, but qualitatively captures thermal discomfort at the scale of neighbourhoods (Figure 6b). The LST Model has low statistical explanatory power, which translates into reduced spatial variation of predicted PET relative to the Selected Model (Figure 6a vs 6c). The LST Model only captures the relative cool thermal comfort adjacent to the large rivers. Finally, LST satellite measurements reveal a pattern that shares some similarity with the PET predicted by the Selected Model, notably in areas adjacent to the large rivers and areas composed of mostly sealed surfaces, but also markedly divergent in other areas such as the old town (Figure 6a vs 6d).
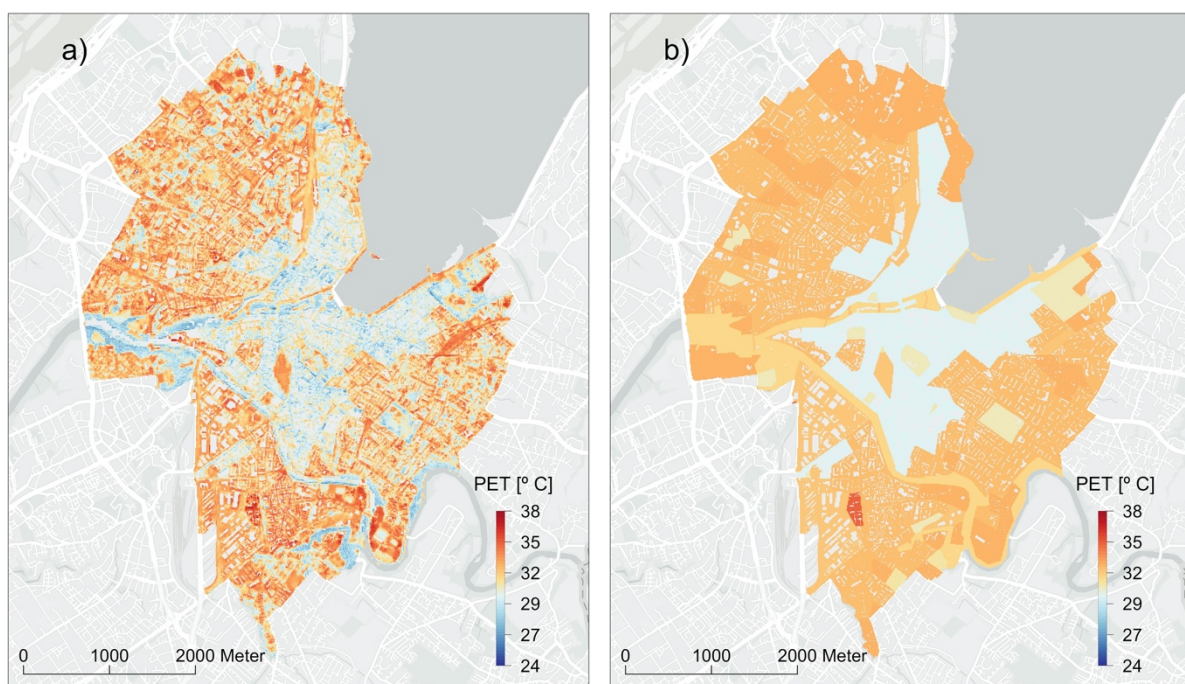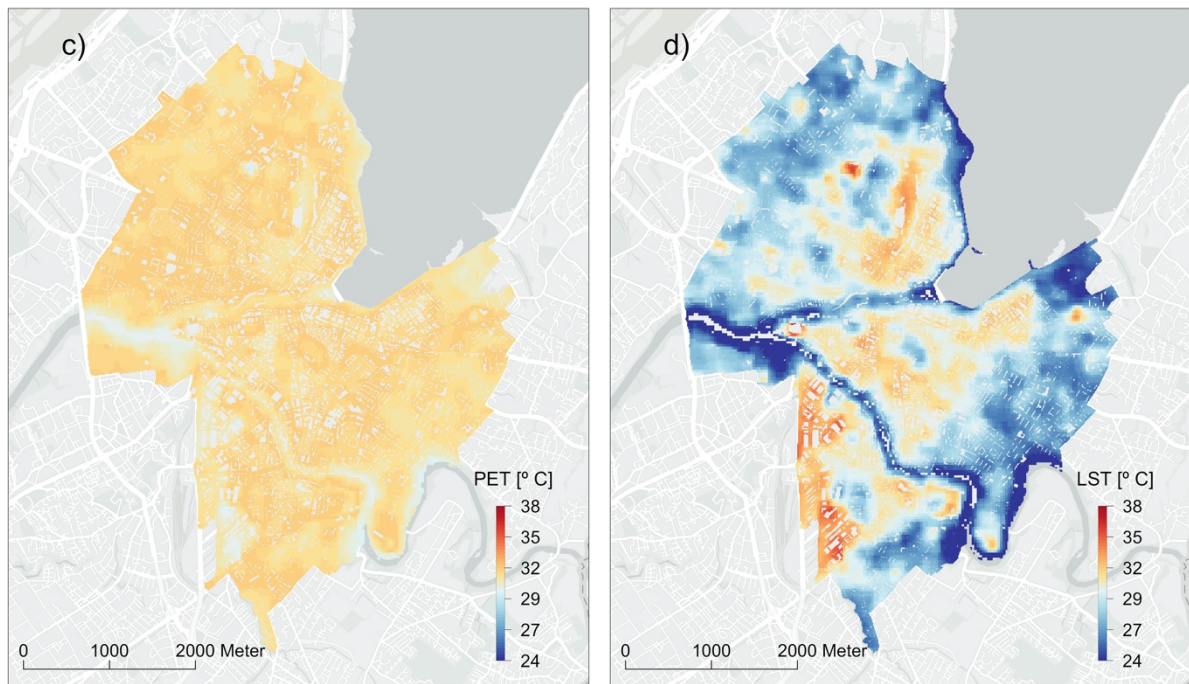
Figure 6: a) Physiological equivalent temperature (PET) based on the Selected GAM, b) predicted with LCZ alone, c) predicted with LST alone, d) measured land surface temperature (LST; average of 14 summer dates, 2015-2018, calculated from Landsat 8 images) in the urban portion of Geneva.

As expected, the spatial distribution of predicted PET from the Selected LMM is very similar to that of the GAM but with a lower explanatory power (Table 4). Just as with the GAMs, PET correlated negatively with LST, NDMI and Canopy cover, and positively with Albedo (Table 4, Table S5). The advantage of the LMM is that it provides an equation for predicting PET (R^2 = 47%), allowing to estimate PET for a city with similar structure as Geneva based on four readily available remote sensing variables (Albedo, LCZ, LST and NDMI; Table S5).

4. Discussion

Reliable predictions of thermal discomfort in urban areas are becoming increasingly important as the fraction of elderly persons increases, and cities are heating up due to densification and climate warming. Here, we show that the spatial variability of PET is large and can be predicted with accuracy in an urban environment using easily accessible remote sensing data. The regression models were constrained and validated using field data gathered with a novel multi-sensor, portable weather instrument that provides an improved estimate of thermal discomfort over air temperature measurements.

The Selected GAM statistically explained the most variance and yielded credible prediction maps of PET in the urban sector for Geneva. According to the variance partitioning, the *LCZ* and *Solar Energy* explained most of the observed variance. The predicted PET in the city centre of Geneva, dominated by LCZ 8 (compact high- and mid-rise buildings, Fig. 4) was lower than in the surrounding suburbs (Fig. 6a). Neighbourhoods with dense buildings thus provide the greatest thermal comfort during the day, outdoors (Shashua-Bar et al., 2012), which contradicts the impression, solely based on LST measurements, that densely built-up urban centres are the warmest and most uncomfortable locations within a city (Figure 6d). The contrasts between PET (Figure 6a) and LST (Figure 6d) also illustrate why LST should not be used to identify and prioritise places subject to diurnal thermal discomfort. For city planning purposes, this suggests that a key pathway for improving well-being in urban environments is increasing the amount of shade through increasing building aspect ratio (building height : street width) (Klok et al., 2019; Lai et al., 2020) – as seen in the old city sections of Mediterranean and North African cities (Negev et al., 2020; Shashua-Bar et al., 2012).

Canopy cover and *NDMI* (Fig S1) also attenuate thermal discomfort (Table 4) (Klok et al., 2019; Lai et al., 2020; Negev et al., 2020; Shashua-Bar et al., 2012). The variance partitioning of the *Selected* GAM model, however, indicates that in Geneva vegetation provides a significant but modest effect on attenuating thermal discomfort, in addition to shading. This

suggests that the recent push to increase the total canopy cover within urban centres will likely help attenuate diurnal thermal comfort while simultaneously adding ecosystem services associated with trees, such as biodiversity support, micro-pollutant interception, reduction of soil erosion and cultural values (Schlaepfer et al., 2020). From a strictly thermal perspective, however, an urban structure with High (>25m tall) to Medium (10-25m tall) buildings (Stewart & Oke, 2012) in close proximity to one another may yield greater results. Our results confirm that areas with low shade due to an absence of building or tall trees do not provide relief from daytime thermal discomfort, even in the presence of low vegetation (LCZ 3, Figure 2)(Klok et al., 2019).

The transects used to collect the PET data were not designed for the purpose of capturing the full variation of PET across the urban fabric and did not include the full urban-rural gradient. Future studies should take care to stratify transects both across and within the most prevalent LCZ types of a given city and a greater diversity of non-urban habitats, and across multiple city morphologies. Indeed, we currently do not know the extent to which these results can be applied to other European and non-European cities. As remote sensing data become increasingly readily available (Skidmore et al., 2021; Vihervaara et al., 2017) field data that can calibrate and validate models will become the limiting factor for developing robust models that can be applied more broadly.

Conclusions

Our study shows that thermal discomfort (PET) can be modelled from readily available remote sensing information, and that LST (both as direct measurements and as a predictor variable) is poorly correlated with daytime outdoor PET (

Figure *6*). Even in full models where LST is a significant predictor, its relative contribution is very modest (Table 5). Our assessment is that LST should not be used to identify neighbourhoods with the highest daytime outdoor thermal discomfort (

Figure *6*). In the absence of field measurements, authorities could use surrogates such as LCZ and remote sensing proxies (Table S5) to target neighbourhoods or micro-environments for remedial measures against thermal discomfort.

Acknowledgements

Author contributions: CRediT

J.C.F. data curation, formal analyses, and writing (original draft); C.B.: formal analyses, visualisation and writing (review and editing); R.C.: funding acquisition, writing (review and editing) and methodology; P.G.: data curation, writing (review and editing); M.A.S. conceptualisation, funding acquisition, project administration, writing (review and editing).

Data availability

Field measurements used to generate PET along transects will be made available on a data repository. All remote sensing data is publicly available.

Funding

References

Alexander, P., & Mills, G. (2014). Local Climate Classification and Dublin's Urban Heat Island. *Atmosphere, 5*, 755-774. https://doi.org/10.3390/atmos5040755

Aminipouri, M., Rayner, D., Lindberg, F., Thorsson, S., Knudby, A. J., Zickfeld, K., Middel, A., & Krayenhoff, E. S. (2019). Urban tree planting to maintain outdoor thermal comfort under climate change: The case of Vancouver's local climate zones. *Building and Environment, 158*, 226-236. https://doi.org/10.1016/j.buildenv.2019.05.022

Anderson, G. F., & Hussey, P. S. (2000). Population Aging: A Comparison Among Industrialized Countries. *Health Affairs, 19*, 191-203. https://doi.org/10.1377/hlthaff.19.3.191

Armstrong, B., et al. (2019). The role of humidity in associations of high temperature with mortality: A multicountry, multicity study. *Environmental Health Perspectives, 127*, 097007. https://doi.org/10.1289/EHP5430

Bartesaghi-Koc, C., Osmond, P., & Peters, A. (2019). Mapping and classifying green infrastructure typologies for climate-related studies based on remote sensing data. *Urban Forestry & Urban Greening, 37*, 154-167. https://doi.org/10.1016/j.ufug.2018.11.008

Blazejczyk, K., Epstein, Y., Jendritzky, G., Staiger, H., & Tinz, B. (2012). Comparison of UTCI to selected thermal indices. *International Journal of Biometeorology, 56*, 515-535. https://doi.org/10.1007/s00484-011-0453-2

Bowler, D. E., Buyung-Ali, L., Knight, T. M., & Pullin, A. S. (2010). Urban greening to cool towns and cities: A systematic review of the empirical evidence. *Landscape and Urban Planning, 97*, 147-155. https://doi.org/10.1016/j.landurbplan.2010.05.006

Bröde, P., Fiala, D., Błażejczyk, K., Holmér, I., Jendritzky, G., Kampmann, B., Tinz, B., & Havenith, G. (2012). Deriving the operational procedure for the Universal Thermal Climate Index (UTCI). *International Journal of Biometeorology, 56*, 481-494. https://doi.org/10.1007/s00484-011-0454-1

Chaudhuri, S., & Kumar, A. (2020). Evaluating the contribution of urban ecosystem services in regulating thermal comfort. *Spatial Information Research, 29*, 71-82. https://doi.org/10.1007/s41324-020-00336-8

Chrysoulakis, N., et al. (2014). A Conceptual List of Indicators for Urban Planning and Management Based on Earth Observation. *ISPRS International Journal of Geo-Information, 3*, 980-1002. https://doi.org/10.3390/ijgi3030980

Coccolo, S., Kämpf, J., Scartezzini, J.-L., & Pearlmutter, D. (2016). Outdoor human comfort and thermal stress: A comprehensive review on models and standards. *Urban Climate, 18*, 33-57. https://doi.org/10.1016/j.uclim.2016.08.004

Deilami, K., Kamruzzaman, M., & Liu, Y. (2018). Urban heat island effect: A systematic review of spatio-temporal factors, data, methods, and mitigation measures. *International Journal of Applied Earth Observation and Geoinformation, 67*, 30-42. https://doi.org/10.1016/j.jag.2017.12.009

Dousset, B., Gourmelon, F., Laaidi, K., Zeghnoun, A., Giraudet, E., Bretin, P., Mauri, E., & Vandentorren, S. (2011). Satellite monitoring of summer heat waves in the Paris metropolitan area. *International Journal of Climatology, 31*, 313-323. https://doi.org/10.1002/joc.2222

Fang, Z., Feng, X., Liu, J., Lin, Z., Mak, C. M., Niu, J., Tse, K.-T., & Xu, X. (2019). Investigation into the differences among several outdoor thermal comfort indices against field survey in subtropics. *Sustainable Cities and Society, 44*, 676-690. https://doi.org/10.1016/j.scs.2018.10.022

Fiala, D., Havenith, G., Bröde, P., Kampmann, B., & Jendritzky, G. (2012). UTCI-Fiala multi-node model of human heat transfer and temperature regulation. *International Journal of Biometeorology, 56*, 429-441. https://doi.org/10.1007/s00484-011-0424-7

Gallinelli, P., Camponovo, R., & Guillot, V. (2017). CityFeel - micro climate monitoring for climate mitigation and urban design. *Energy Procedia, 122*, 391-396. https://doi.org/10.1016/j.egypro.2017.07.427

Geletič, J., Lehnert, M., Savić, S., & Milošević, D. (2018). Modelled spatiotemporal variability of outdoor thermal comfort in local climate zones of the city of Brno, Czech Republic. *Science of the Total Environment, 624*, 385-395. https://doi.org/10.1016/j.scitotenv.2017.12.076

Gulyás, Á., Unger, J., & Matzarakis, A. (2006). Assessment of the microclimatic and human comfort conditions in a complex urban environment: Modelling and measurements. *Building and Environment, 41*, 1713-1722. https://doi.org/10.1016/j.buildenv.2005.07.001

He, X., Miao, S., Shen, S., Li, J., Zhang, B., Zhang, Z., & Chen, X. (2015). Influence of sky view factor on outdoor thermal environment and physiological equivalent temperature. *International Journal of Biometeorology, 59*, 285-297. 10.1007/s00484-014-0841-5

Höppe, P. (1999). The physiological equivalent temperature – a universal index for the biometeorological assessment of the thermal environment. *International Journal of Biometeorology, 43*, 71-75. https://doi.org/10.1007/s004840050118

Huang, W. T. K., Masselot, P., Bou-Zeid, E., Fatichi, S., Paschalis, A., Sun, T., Gasparrini, A., & Manoli, G. (2023). Economic valuation of temperature-related mortality attributed to urban heat islands in European cities. *Nature Communications, 14*, 7438. https://doi.org/10.1038/s41467-023-43135-z

Iungman, T., et al. (2023). Cooling cities through urban green infrastructure: a health impact assessment of European cities. *The Lancet*, https://doi.org/10.1016/S0140-6736(22)02585-5. https://doi.org/10.1016/S0140-6736(22)02585-5

Kakon, A. N., Nobuo, M., Kojima, S., & Yoko, T. (2010). Assessment of Thermal Comfort in Respect to Building Height in a High-Density City in the Tropics. *American Journal of Engineering and Applied Sciences, 3*. https://doi.org/10.3844/ajeassp.2010.545.551

Kamath, H. G., Martilli, A., Singh, M., Brooks, T., Lanza, K., Bixler, R. P., Coudert, M., Yang, Z.-L., & Niyogi, D. (2023). Human heat health index (H3I) for holistic assessment of heat hazard and mitigation strategies beyond urban heat islands. *Urban Climate, 52*, 101675. https://doi.org/10.1016/j.uclim.2023.101675

Klok, L., Rood, N., Kluck, J., & Kleerekoper, L. (2019). Assessment of thermally comfortable urban spaces in Amsterdam during hot summer days. *International Journal of Biometeorology, 63*, 129-141. https://doi.org/10.1007/s00484-018-1644-x

Kundu, D., & Pandey, A. K. (2020). World Urbanisation: Trends and Patterns. In D. Kundu, R. Sietchiping, & M. Kinyanjui (Eds.), *Developing National Urban Policies: Ways Forward to Green and Smart Cities* (10.1007/978-981-15-3738-7_2pp. 13-49). Springer Nature Singapore. https://doi.org/10.1007/978-981-15-3738-7_2

Lai, D., Lian, Z., Liu, W., Guo, C., Liu, W., Liu, K., & Chen, Q. (2020). A comprehensive review of thermal comfort studies in urban open spaces. *Science of the Total Environment, 742*, 140092. https://doi.org/10.1016/j.scitotenv.2020.140092

Lehmann, I., Mathey, J., Rossler, S., Brauer, A., & Goldberg, V. (2014). Urban vegetation structure types as a methodological approach for identifying ecosystem services - Application to the analysis of micro-climatic effects. *Ecological Indicators, 42*, 58-72. https://doi.org/10.1016/j.ecolind.2014.02.036

Liu, L., Lin, Y., Xiao, Y., Xue, P., Shi, L., Chen, X., & Liu, J. (2018). Quantitative effects of urban spatial characteristics on outdoor thermal comfort based on the LCZ scheme. *Building and Environment, 143*, 443-460. https://doi.org/10.1016/j.buildenv.2018.07.019

Makido, Y., Hellman, D., & Shandas, V. (2019). Nature-Based Designs to Mitigate Urban Heat: The Efficacy of Green Infrastructure Treatments in Portland, Oregon. *Atmosphere, 10*, 282. https://doi.org/10.3390/atmos10050282

May, S., & Oliphant, A. J. (2023). Characteristics of the Park Cool Island in Golden Gate Park, San Francisco. *Theoretical and Applied Climatology, 151*, 1269-1282. https://doi.org/10.1007/s00704-022-04296-x

Negev, M., Khreis, H., Rogers, B. C., Shaheen, M., & Erell, E. (2020). City design for health and resilience in hot and dry climates. *BMJ, 371*, m3000. https://doi.org/10.1136/bmj.m3000

Oke, T. R. (1982). The energetic basis of the urban heat island. *Quarterly Journal of the Royal Meteorological Society, 108*, 1-24. https://doi.org/10.1002/qj.49710845502

Oke, T. R., Mills, G., Christen, A., & Voogt, J. A. (2017). *Urban Climates* (https://doi.org/10.1017/9781139016476). Cambridge University Press.

Ormandy, D., & Ezratty, V. (2016). Thermal discomfort and health: protecting the susceptible from excess cold and excess heat in housing. *Advances in Building Energy Research, 10*, 84-98. https://doi.org/10.1080/17512549.2015.1014845

Parlow, E., Vogt, R., & Feigenwinter, C. (2014). The urban heat island of Basel – seen from different perspectives. *DIE ERDE – Journal of the Geographical Society of Berlin, 145*, 96-110. https://doi.org/10.12854/erde-145-8

Potchter, O., Cohen, P., Lin, T.-P., & Matzarakis, A. (2018). Outdoor human thermal perception in various climates: A comprehensive review of approaches, methods and quantification. *Science of the Total Environment, 631-632*, 390-406. https://doi.org/10.1016/j.scitotenv.2018.02.276

R core team. (2023). *R: A language and environment for statistical computing.* .R Foundation for Statistical Computing.

Ragettli, M. S., Vicedo-Cabrera, A. M., Schindler, C., & Röösli, M. (2017). Exploring the association between heat and mortality in Switzerland between 1995 and 2013. *Environmental Research, 158*, 703-709. https://doi.org/10.1016/j.envres.2017.07.021

Ray-Mukherjee, J., Nimon, K., Mukherjee, S., Morris, D. W., Slotow, R., & Hamer, M. (2014). Using commonality analysis in multiple regressions: a tool to decompose regression effects in the face of multicollinearity. *Methods in Ecology and Evolution, 5*, 320-328. https://doi.org/10.1111/2041-210X.12166

Sadeghipour Roudsari, M. (2024). *PET Comfort*. Retrieved 12 june 2024 from https://docs.ladybug.tools/ladybug-primer/components/1_analyzedata/pet_comfort

Santamouris, M. (2014). Cooling the cities – A review of reflective and green roof mitigation technologies to fight heat island and improve comfort in urban environments. *Solar Energy, 103*, 682-703. https://doi.org/10.1016/j.solener.2012.07.003

Schlaepfer, M. A., Guinaudeau, B. P., Martin, P., & Wyler, N. (2020). Quantifying the contributions of native and non-native trees to a city's biodiversity and ecosystem services. *Urban Forestry & Urban Greening, 56*, 126861. https://doi.org/10.1016/j.ufug.2020.126861

Schwaab, J., Davin, E. L., Bebi, P., Duguay-Tetzlaff, A., Waser, L. T., Haeni, M., & Meier, R. (2020). Increasing the broad-leaved tree fraction in European forests mitigates hot temperature extremes. *Scientific Reports, 10*, 14153. https://doi.org/10.1038/s41598-020-71055-1

Shashua-Bar, L., & Hoffman, M. E. (2000). Vegetation as a climatic component in the design of an urban street: An empirical model for predicting the cooling effect of urban green areas with trees. *Energy and Buildings, 31*, 221-235. https://doi.org/10.1016/S0378-7788(99)00018-3

Shashua-Bar, L., Tsiros, I. X., & Hoffman, M. (2012). Passive cooling design options to ameliorate thermal comfort in urban streets of a Mediterranean climate (Athens) under hot summer conditions. *Building and Environment, 57*, 110-119. https://doi.org/10.1016/j.buildenv.2012.04.019

Skidmore, A. K., et al. (2021). Priority list of biodiversity metrics to observe from space. *Nat Ecol Evol*, https://doi.org/10.1038/s41559-021-01451-x. https://doi.org/10.1038/s41559-021-01451-x

Stewart, I. D., & Oke, T. R. (2012). Local Climate Zones for Urban Temperature Studies. *Bulletin of the American Meteorological Society, 93*, 1879-1900. https://doi.org/10.1175/bams-d-11-00019.1

Stewart, I. D., Oke, T. R., & Krayenhoff, E. S. (2014). Evaluation of the 'local climate zone' scheme using temperature observations and model simulations. *International Journal of Climatology, 34*, 1062-1080. https://doi.org/10.1002/joc.3746

Tomlinson, C. J., Chapman, L., Thornes, J. E., & Baker, C. (2011). Remote sensing land surface temperature for meteorology and climatology: a review. *Meteorological Applications, 18*, 296-306. https://doi.org/10.1002/met.287

van Hove, L. W. A., Jacobs, C. M. J., Heusinkveld, B. G., Elbers, J. A., van Driel, B. L., & Holtslag, A. A. M. (2015). Temporal and spatial variability of urban heat island and thermal comfort within the Rotterdam agglomeration. *Building and Environment, 83*, 91-103. https://doi.org/10.1016/j.buildenv.2014.08.029

Venter, Z. S., Krog, N. H., & Barton, D. N. (2020). Linking green infrastructure to urban heat and human health risk mitigation in Oslo, Norway. *Science of the Total Environment, 709*, 136193. https://doi.org/10.1016/j.scitotenv.2019.136193

Vihervaara, P., et al. (2017). How Essential Biodiversity Variables and remote sensing can help national biodiversity monitoring. *Global Ecology and Conservation, 10*, 43-59. https://doi.org/10.1016/j.gecco.2017.01.007

Voogt, J. A., & Oke, T. R. (2003). Thermal remote sensing of urban climates. *Remote Sensing of Environment, 86*, 370-384. https://doi.org/10.1016/S0034-4257(03)00079-8

Walther, E., & Goestchel, Q. (2018). The P.E.T. comfort index: Questioning the model. *Building and Environment, 137*, 1-10. https://doi.org/10.1016/j.buildenv.2018.03.054

Weng, Q., Lu, D., & Schubring, J. (2004). Estimation of land surface temperature–vegetation abundance relationship for urban heat island studies. *Remote Sensing of Environment, 89*, 467-483. https://doi.org/10.1016/j.rse.2003.11.005

Zare, S., Hasheminejad, N., Shirvan, H. E., Hemmatjo, R., Sarebanzadeh, K., & Ahmadi, S. (2018). Comparing Universal Thermal Climate Index (UTCI) with selected thermal indices/environmental parameters during 12 months of the year. *Weather and Climate Extremes, 19*, 49-57. https://doi.org/10.1016/j.wace.2018.01.004

Zhang, K., Li, Y., Schwartz, J. D., & O'Neill, M. S. (2014). What weather variables are important in predicting heat-related mortality? A new application of statistical learning methods. *Environ Res, 132*, 350-359. https://doi.org/10.1016/j.envres.2014.04.004

Supplementary Materials

Fahy et al. Beyond land surface temperature: identifying areas of daytime thermal discomfort in cities by combining remote sensing and field measurements.

Table S6: Measured variables and corresponding sensors on the portable climate station

Notes S1: Methodological information on spatial data acquisition and preparation.

Figure S1. Maps of explanatory variables used in PET models

Figure S2: Correlation between the physiological equivalent temperature (PET) and air temperature (Tair) and land surface temperature (LST)

Figure S3: Correlation between the normalised difference vegetation index (NDVI) and the normalised difference moisture index (NDMI)

Table S2: GAM Model outputs

Table S3: GAM model output with tensor spline

Table S4: LLM model outputs

Table S5: LMM predictive equations for PET based on *Selected* and *Easy Access* models

Table S7: Measured variables and corresponding sensors on the portable climate station.

Parameter	Probe/sensor type	Resolution / Error
Position (time, dd, m, ms, °)	GNSS receiver	0.1m / typical 5m
Heading (°)	Magnetic field sensor	1° / 2°
Air temperature ref. (°C)	Band gap temperature sensor	0.1°C / 0.1°C
Air temperature other (°C)	PT100	0.1°C / 0.2°C
Humidity (%)	Capacitive humidity sensor	0.1% / 1%
Surface temperatures (°C)	Digital Non-Contact Infrared Thermometers	0.1°C / 0.5°C
Solar irradiance (°C)	Photodiode Pyranometer	1 W/m² / 1.5%
Sound level (dB(A))	Sound level meter	1dB / 3%
Fine particulate matter (μg/m^3)	Laser sensor	1mg/m³ / 10%
CO_2 (ppm)	NDIR sensor	30ppm / 3%
NO_2, O_3, SO_2, CO (ppb)	Chemical sensor	+/- 2ppb / 20%
Wind speed and direction (m/s and °)	Ultrasonic anemometer	0.01m/s / 1%
Photograph	FishEye Camera module	VGA

Notes S1: Methodological information on spatial data acquisition and preparation.

Microclimate meter: Surface temperatures are used to calculate mean radiant temperature (MRT). The Tsurf sensor array is set up to measure surface temperatures in six cardinal directions using industrial precision bolometers. MRT is derived using the formula in ISO 7726 and applying shape factors derived from VDI_3787_Part-2 page 29, typical of a standing person. In addition, shortwave radiation (Gh) is monitored on a horizontal plane to assess incoming global solar radiation. In this way we can distinguish MRT with and without the direct solar component. In comparison, the MaRTy (Middel & Krayenhoff, 2019) setup uses the net radiometer method using photopile pyranometers and pyrgeometers. These are suitable for static measurements, having a 95% response time of several seconds, whilst the longwave bolometers used to evaluate surface temperatures used in the microclimate-meter setup give and immediate feedback (response time less than 200 ms) required to accurately asses rapid variations during mobile transects at pedestrian speed (1-2 m/s) (Gallinelli et al., 2017).

Remote sensing data:

Evapotranspiration data was obtained from MODIS (https://modis.gsfc.nasa.gov/data/dataprod/mod16.php) for the period 28.07.2019-04.08.2019.

Mean summer LST values were calculated from fourteen Landsat 8 images taken between June 20 and September 10 of the years 2015 to 2018. Only satellite images with less than 5% of cloud cover over the canton of Geneva were selected. As recommended by USGS (2019), we did not retrieve band 11 (thermal infrared 2) of Landsat 8 because it is associated with a larger calibration uncertainty than band 10 (thermal infrared 1). For this reason, we undertook a single-window algorithm. The equation to estimate L_{ST} comes from Weng (2004):

$$L_{ST} = BT / (1 + (\lambda * BT / \rho) * \ln(\varepsilon))$$

where BT = brightness temperature (K); λ = wavelength of emitted radiance (10.8 μm for band 10 of Landsat 8); ρ = 14380 μm K, see Weng et al. (p. 472Weng et al., 2004); and ε = emissivity. The result was converted from degrees Kelvin to Celsius.

Emissivity (in the formula for L_{ST}) is estimated indirectly with the NDVI (Normalized Difference Vegetation Index) method described in Weng (2004) and based on Liu and Zhang (2011). This method is preferred over ASTER and MODIS emissivity products because of its simplicity and its higher resolution of 30 x 30 m (Parastatidis et al., 2017).

NDMI and NDVI are indices that capture atmospheric moisture and photosynthetic activity, respectively. These two indices were directly calculated in Google Earth Engine (GEE) using Sentinel-2 images from summer 2019, with the following equations:

NDMI = (NIR – SWIR2) / (NIR + SWIR2)

NDVI = (NIR-RED) / (NIR+RED)

Shortwave broadband albedo was calculated in GEE with Sentinel-2 surface reflectance images of summer 2019 using Liang's (2001) equation from Naegeli et al. (2017):

α = 0.356 Blue + 0.130 Red + 0.373 NIR + 0.085 SWIR1 + 0.072 SWIR2− 0.0018

Solar energy is represented by the sum of solar irradiance in July (kWh/m^2) and is obtained from a public geospatial repository (https://ge.ch/sitg/fiche/6644). It incorporates shading from topography, adjacent buildings and vegetation.

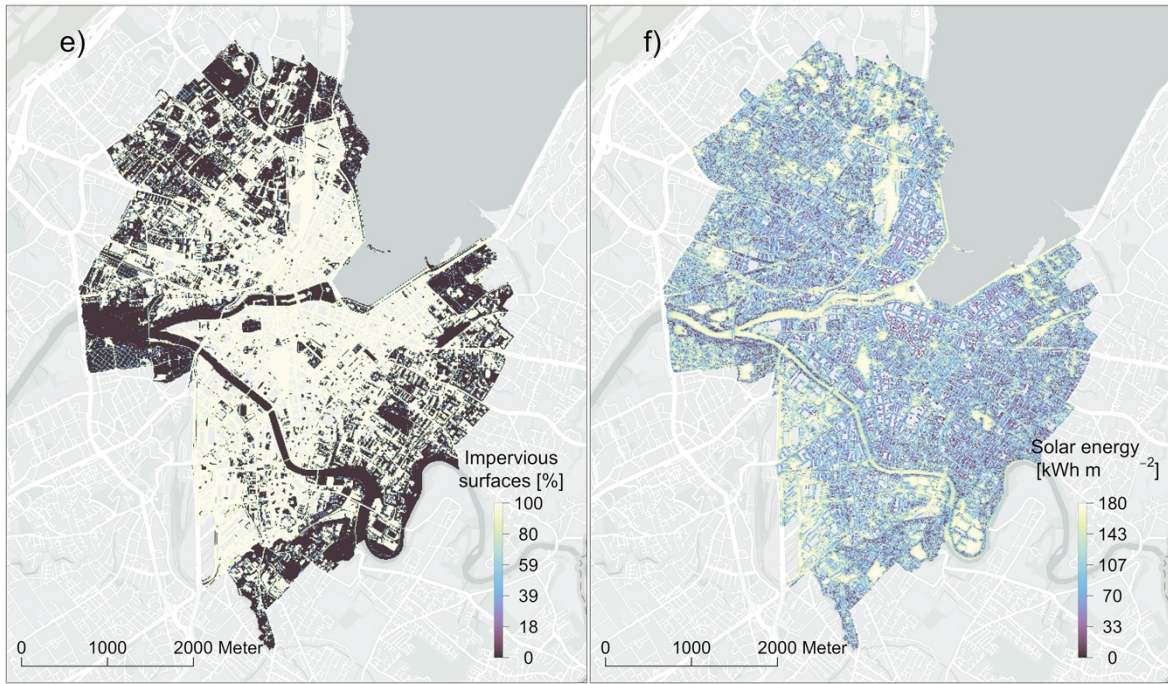**Figure S1**. Maps of explanatory variables used in PET models
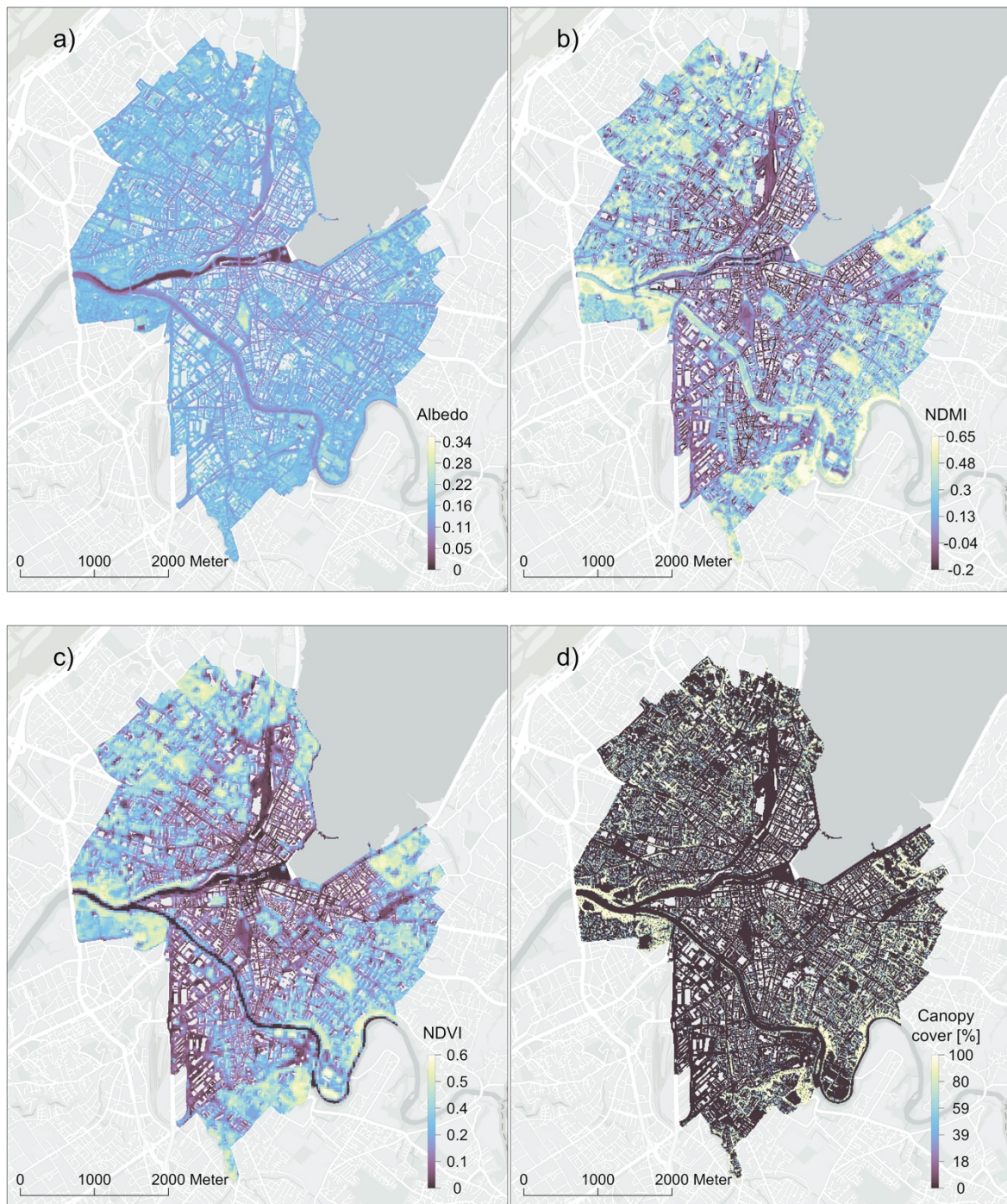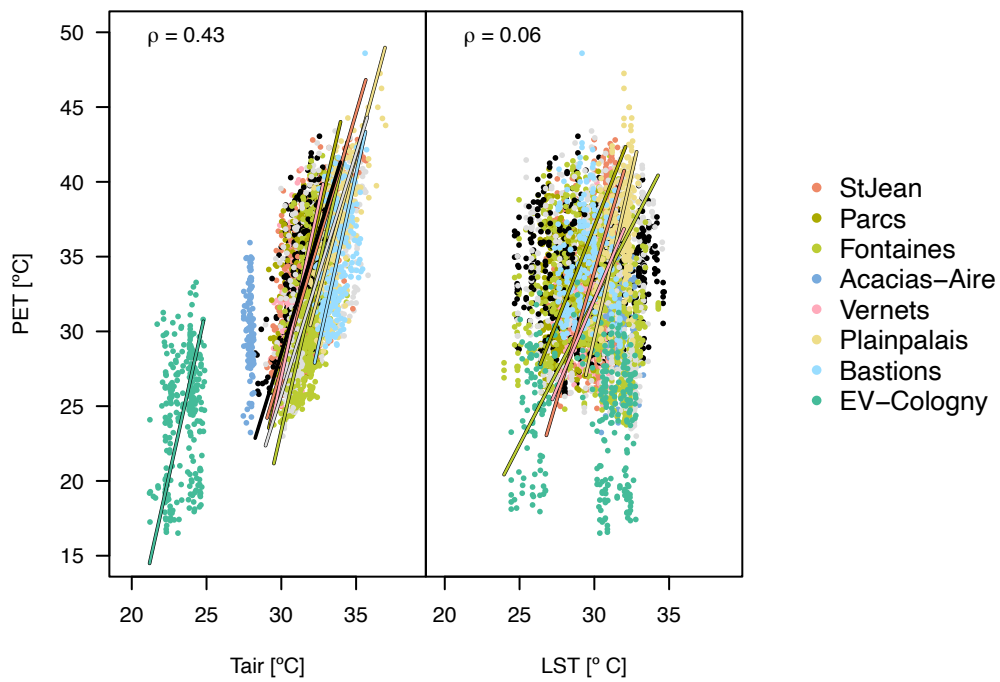
Figure S2: Correlation between the physiological equivalent temperature (PET) and air temperature (T_{air}) and land surface temperature (LST), respectively. Geometric regression lines are shown for the significant correlations ($p < 0.05$) for each transect and date separately, spearman correlations (ρ) are means of the individual correlation coeficients.
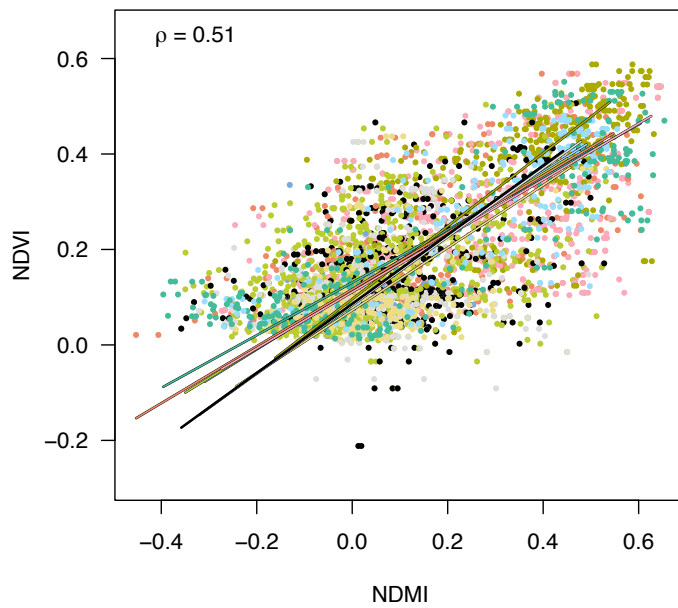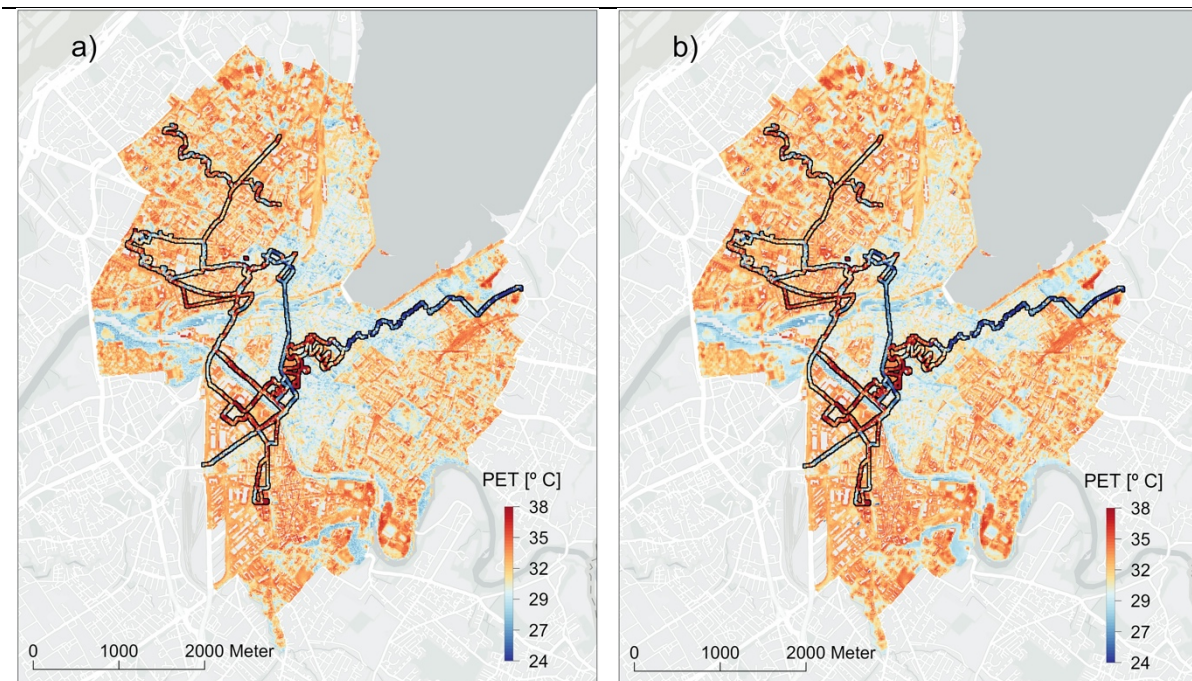
Figure S3: Correlation between the normalised difference vegetation index (NDVI) and the normalised difference moisture index (NDMI) across all transects and dates. The pearson correlation shows the mean of the correlation coefficients.
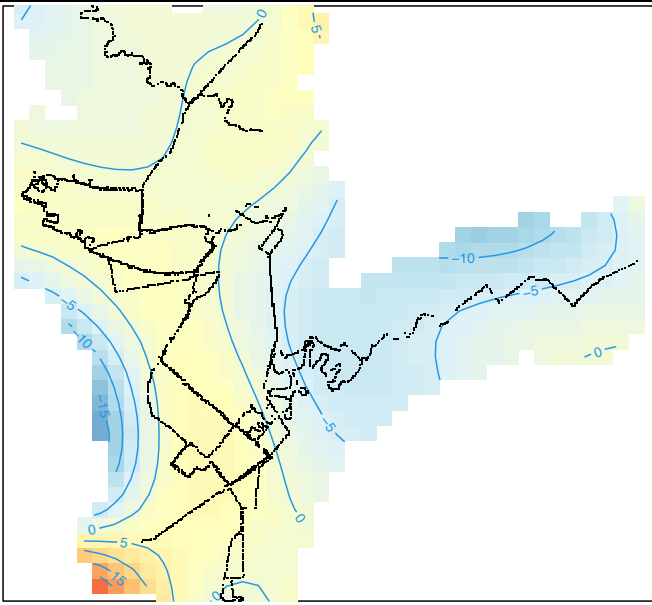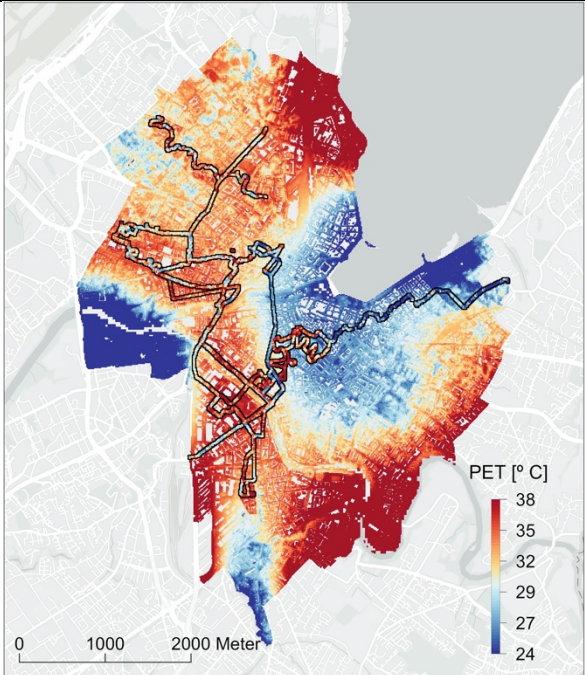
Figure S4: *Selected* and *Easy access* GAM outputs

Model *Selected*   Model E*asy access*

Table S3: *Selected* GAM and LMM output with tensor spline

Model formula	Goodness of fit	tensor spline	prediction map
Selected GAM + tensor spline	R^2 = 51.3 % RMSE = 3.29 Percent bias = 0.01 NS efficiency = 0.45		

Selected LMM	fixed effects: 2.7 %	
	random effects: 46.3 %	
+ tensor spline	RMSE = 3.69	
	Percent bias = 0.01	
	NS efficiency = 0.31	
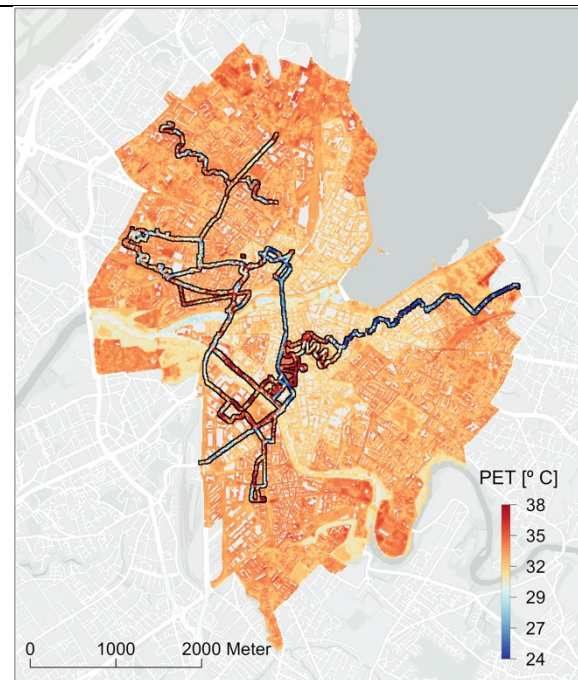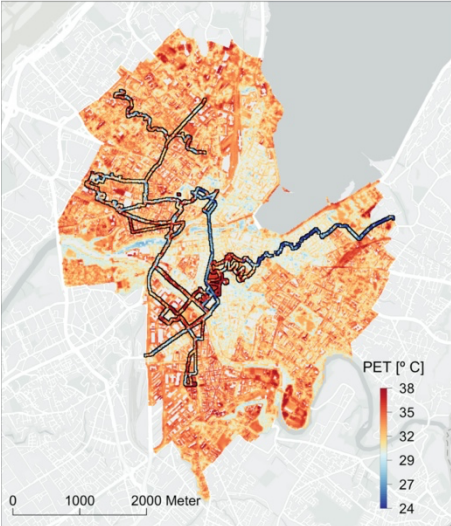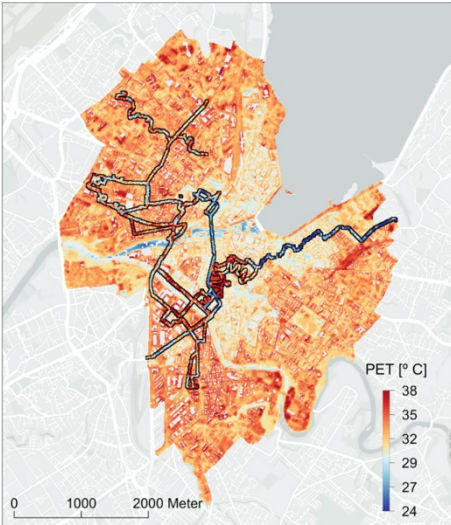
Table S4: LLM outputs.

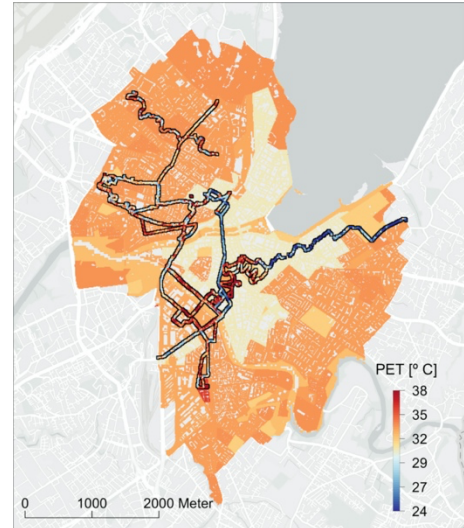| Model formula	Goodness of fit	prediction map
Selected model	R^2_{fixed} = 11.1 % R^2_{total} = 48.0 % RMSE = 3.61 Percent bias = 0.01 NS efficiency = 0.34	
Easy access model	R^2_{fixed} = 9.3 % R^2_{total} = 47.0 % RMSE = 3.66 Percent bias = -0.01 NS efficiency = 0.33	

LCZ alone

R^2_{fixed} = 5.4 %

R^2_{total} = 45.9 %

RMSE = 3.78

Percent bias = 0.01

NS efficiency = 0.28

LST alone

R^2_{fixed} < 0.1 %

R^2_{total} = 41.9 %

RMSE = 3.77

Percent bias = 0.01
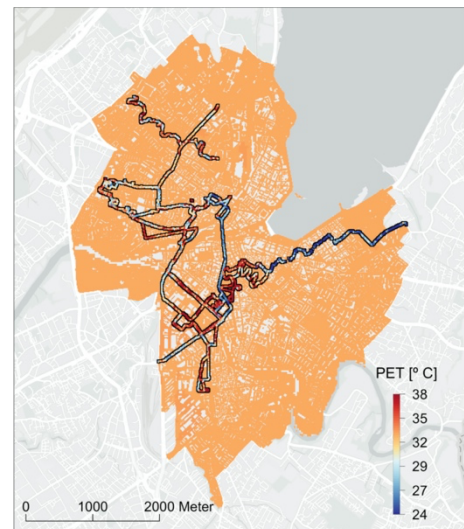
NS efficiency = 0.28

Table S5: LMM predictive equations for PET based on *Selected* and *Easy Access* models

Variables:

PET is the Physiological Equivalent Temperature (C°) per 10m x 10m cell

Canopy Cover is the % canopy cover

LST is Land Surface Temperature in °C

NDMI [-1, +1]

Solar Energy, which the monthly sum of irradiance during the month of July
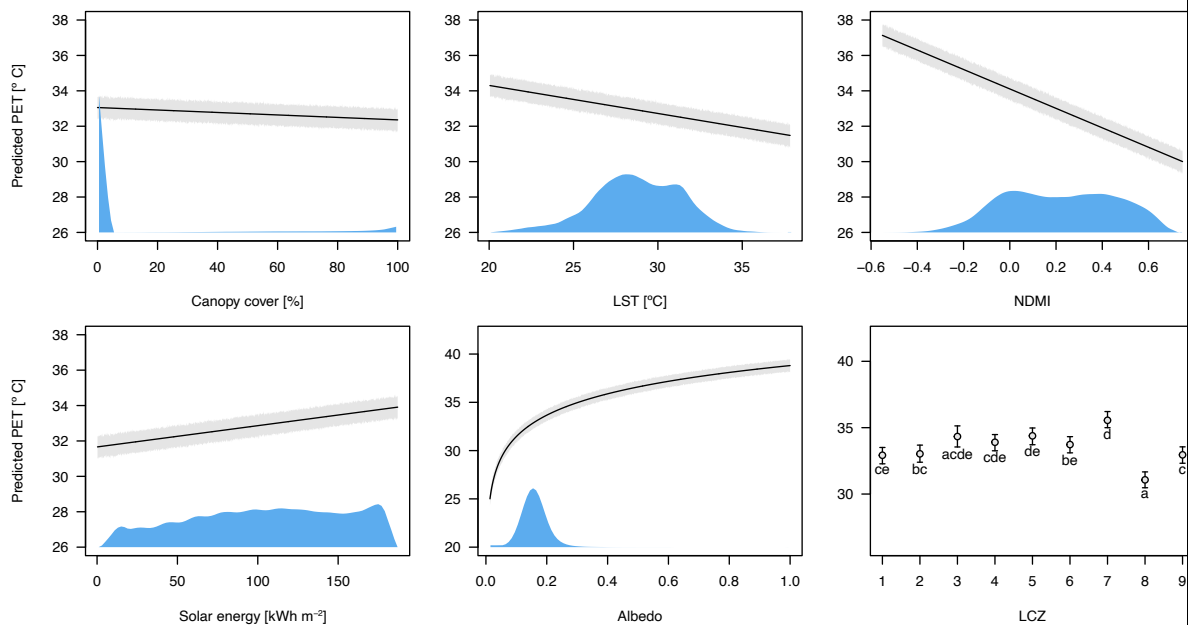
Albedo [0, +1]

LCZ type is based on merged LCZ categories (see Table 3)

Model *Selected* (total R^2 = 48%):

PET = 42.45 - 0.00698 * canopy_cover - 0.158 * LST - 5.49 * NDMI + 0.012 * Solar Energy

+ 3.19 * ln(albedo) + LCZ

Where LCZ is a correction factor that varies as a function of the LCZ type:

LCZ 1: 0, LCZ 2: + 0.108, LCZ 3: + 1.412, LCZ 4: + 0.979 , LCZ 5: + 1.462, LCZ 6: +

0.806, LCZ 7: + 2.633, LCZ 8: - 1.851, LCZ 9: + 0.030

Predicted PET over the range of the six explanatory variables (plus minus prediction s.e.

interval in grey) for the selected LMM model. The blue areas show the density distribution

of the predictors across their interval. Letters indicate pairwise comparisons of the effect of LCZ (p < 0.05). Note that the y axis differs for albedo.

Model *Easy Access* (total $R^2 = 47\%$):

PET $\sim$ 45.97 - 0.177 * LST -6.42 * NDMI + 3.95 * ln(albedo) + LCZ

Where, LCZ is a correction factor that varies as a function of the LCZ number (see Table 3 in main text for correspondence with LCZ categories):

LCZ 1: 0, LCZ 2: - 0.146, LCZ 3: + 2.095, LCZ 4: + 0.934, LCZ 5: +1.291, LCZ 6: + 0.641, LCZ 7: + 2.199, LCZ 8: - 1.969, LCZ 9 + 0.138

Literature Cited:

Gallinelli, P., Camponovo, R., & Guillot, V. (2017). CityFeel - micro climate monitoring for climate mitigation and urban design. *Energy Procedia, 122*, 391-396. https://doi.org/10.1016/j.egypro.2017.07.427

Liang, S. (2001). Narrowband to broadband conversions of land surface albedo I. *Remote Sensing of Environment, 76*, 213-238. 10.1016/S0034-4257(00)00205-4

Liu, L., & Zhang, Y. (2011). Urban Heat Island Analysis Using the Landsat TM Data and ASTER Data: A Case Study in Hong Kong. *Remote Sensing, 3*, 1535-1552. 10.3390/rs3071535

Middel, A., & Krayenhoff, E. S. (2019). Micrometeorological determinants of pedestrian thermal exposure during record-breaking heat in Tempe, Arizona: Introducing the MaRTy observational platform. *Science of the Total Environment, 687*, 137-151. https://doi.org/10.1016/j.scitotenv.2019.06.085

Naegeli, K., Damm, A., Huss, M., Wulf, H., Schaepman, M., & Hoelzle, M. (2017). Cross-Comparison of Albedo Products for Glacier Surfaces Derived from Airborne and Satellite (Sentinel-2 and Landsat 8) Optical Data. *Remote Sensing, 9*, 110. 10.3390/rs9020110

Parastatidis, D., Mitraka, Z., Chrysoulakis, N., & Abrams, M. (2017). Online Global Land Surface Temperature Estimation from Landsat. *Remote Sensing, 9*, 1208. https://www.mdpi.com/2072-4292/9/12/1208

USGS. (2019). *Landsat 8 (L8) Data Users Handbook.* U. S. G. S. Department of the Interior.

Weng, Q., Lu, D., & Schubring, J. (2004). Estimation of land surface temperature–vegetation abundance relationship for urban heat island studies. *Remote Sensing of Environment, 89*, 467-483. https://doi.org/10.1016/j.rse.2003.11.005